RESEARCH ARTICLE

ADVANCED PHYSICS RESEARCH Open Access

www.advphysicsres.com

Impurity Band Formation as a Route to Thermoelectric Power Factor Enhancement in n-type XNiSn Half-Heuslers

Robert J. Quinn, Yuji Go, Aaron B. Naden, Andras Bojtor, Gabor Paráda, Ashiq K. M. A. Shawon, Kamil Domosud, Keith Refson, Alexandra Zevalkink, Neophytos Neophytou, and Jan-Willem G. Bos**

Bandstructure engineering is a key route for thermoelectric performance enhancement. Here, 20–50% Seebeck (*S*) enhancement is reported for $XNiCu_ySn$ half-Heusler samples based on X = Ti. This novel electronic effect is attributed to the emergence of impurity bands of finite extent, due to the Cu dopants. Depending on the dispersion, extent, and offset with respect to the parent material, these bands are shown to enhance *S* to different degrees. Experimentally, this effect is controllable by the Ti content of the samples, with the addition of Zr/Hf gradually removing the enhancement. At the same time, the mobility remains largely intact, enabling power factors ≥3 mW m^{-1} K^{-2} near room temperature, increasing to ≥5 mW m^{-1} K^{-2} at high temperature. Combined with reduced thermal conductivity due to the Cu interstitials, this enables high average zT = 0.67–0.72 between 320 and 793 K for $XNiCu_ySn$ compositions with ≥70% Ti. This work reveals the existence of a new route for electronic performance enhancement in n-type XNiSn materials that are normally limited by their single carrier pocket. In principle, impurity bands can be applied to other materials and provide a new direction for further development.

1. Introduction

Thermoelectric (TE) devices use semiconductor materials to convert heat and electricity with key advantages including high reliability, low electronic noise, and scalability.[1] Current applications include power generation for space exploration and cooling of advanced optical components.[2] TEs have great promise for energy sustainability in power generation from industrial waste heat and in scavenging, for example reducing reliance on batteries in sensors for the Internet of Things or in self-powered medical diagnostics.[1a,3]

The most efficient TEs are metal chalcogenides, including Bi_2Te_3, PbTe, SnSe, and GeTe based alloys, which at high temperatures have $zT > 2$,[4] Here, $zT = S^2\sigma T/\kappa$, is the TE figure of merit.[1d] This metric combines three key bulk materials properties, namely the Seebeck coefficient (S), the electrical conductivity (σ), and the thermal conductivity (κ), which is the sum of the lattice (κ_L) and electronic (κ_E) thermal conductivity. The numerator $S^2\sigma$, is the TE power factor (PF) and is a measure of the power generation potential of a TE material.[5]

Half-Heusler (HH) materials are one of the leading contenders for application in power generation and thermal management, despite lower zT values. This is driven by their good electrical properties, low toxicity, and favorable engineering properties, such as good mechanical strength, temperature stability, and ease of making electrical contacts in devices.[6]

A wide variety of HH families have been investigated, with benchmark $zT \geq 1$ found for n-type compositions based on

R. J. Quinn
Institute of Chemical Sciences
School of Engineering and Physical Sciences
Heriot-Watt University
Edinburgh EH14 4AS, UK

The ORCID identification number(s) for the author(s) of this article can be found under https://doi.org/10.1002/apxr.202400179

[Correction added on January 25 2025 after first online publication: the second author's name was corrected in this version.]

DOI: 10.1002/apxr.202400179

Y. Go, N. Neophytou
School of Engineering
University of Warwick
Coventry CV4 7AL, UK
E-mail: N.Neophytou@warwick.ac.uk

A. B. Naden, J.-W. G. Bos
EaStCHEM School of Chemistry
University of St Andrews
North Haugh, St Andrews KY16 9ST, UK
E-mail: j.w.g.bos@st-andrews.ac.uk

A. Bojtor, G. Paráda
Semilab Co. Ltd.
4/A Prielle Kornélia, Budapest 1117, Hungary

A. K. M. A. Shawon, A. Zevalkink
Chemical Engineering and Materials Science Department
Michigan State University
East Lansing, Michigan 48824, USA

ZrNiSn[7] and $Nb_{0.8}CoSb$,[8] and p-types including ZrCoSb,[9] NbFeSb[10] and ZrCoBi.[11] Typically, these materials are optimized using alloying with heavy elements, for example mixing Zr and Hf in the case of ZrNiSn, which primarily serves to suppress κ_L. Here, the small size difference of the alloying elements due to the lanthanide contraction is considered essential to maintain good electron mobilities.[7f,10d] In addition, dopants are used to control the charge carrier concentration, for example, Sb^{3-} for Sn^{4-} in ZrNiSn and Ti^{4+} for Nb^{5+} in NbFeSb. Beyond alloying and doping, bandstructure engineering is a key route for performance enhancement. Here, the p-type HH materials benefit from complex valence band structures with multiple carrier pockets. In case of p-type NbFeSb and ZrCoSb/Bi, composition design, to tune the band mass, and achieve band convergence has been used to improve the *PF*.[10h,i,11b] By contrast, in the n-type XNiSn system, a single carrier pocket at the X point contributes to the electrical transport, thus there is limited scope for bandstructure engineering.[12]

In this work, we present a new mechanism for *S* and *PF* performance enhancement that could address the single pocket band limitations of the XNiSn system. This effect is linked to the presence of dopant-derived impurity bands. It occurs in the $XNiCu_ySn$ system and is strongest for compositions with ≥70% Ti, contrasting with the usual focus on Zr/Hf compositions. Here, interstitial Cu is used as a dopant but simultaneously modifies the electronic structure, leading to a fracturing of the conduction band. We propose that this band fracturing is the key feature that explains the observed enhanced *S* and *PF*. A minimal model incorporating dopant-derived bands of finite extent, in addition to the parent material conduction band, can explain the observed experimental trends. The carrier mobility is only mildly affected, enabling 50% *PF* improvements to >3 mW m^{-1} K^{-2} (for Ti-based samples) near room temperature. At high-temperature, the performance advantage of the Ti-based samples is somewhat less, but they continue to have the largest *PF* exceeding 4.5 mW m^{-1} K^{-2}. Combined with low thermal conductivities and alloying optimization this *PF* enhancement supports high average $zT = 0.67$–0.72 between 320 and 793 K. These results point toward a novel band/defect-engineering direction that can be applied to other materials.

2. Results

2.1. Cu Interstitials in XNiSn Materials

The use of Cu interstitials in XNiSn materials has attracted only limited interest compared to using separate dopants and alloying elements.[13] Detailed structural analysis, including neutron powder diffraction,[13b–d] electron microscopy[13b,c], and atom probe tomography,[14] has been used to demonstrate that Cu is largely homogeneously distributed in XNiSn samples. Most of the Cu is found to occupy the normally vacant 4d site in the crystal structure with some Cu segregation occurring at grain boundaries. The atomic arrangement within the $XNiCu_ySn$ unit cell is shown in **Figure 1a**. Figure 1b–e visualizes the segregation of Cu at grain boundaries and as small Cu inclusions for a $TNiCu_{0.03}Sn$ sample prepared for this study. The TEM data also illustrates the generally highly ordered structure without extended defects. In terms of TE performance, each Cu donates a single electron (i.e., the same as Sb) and is a strong phonon scatterer with values as low as 4 W m^{-1} K^{-1} at room temperature in $TiNiCu_ySn$ ($y = 0.02$–0.05).[13b,c] However, the Cu dopants also influence the electronic properties beyond carrier doping.[13c]

Already in earlier work, the presence of a large Density of States (DOS) mass, m^*_{DOS} ≈4.2 m_e from the use of the single parabolic band (SPB) analysis and Pisarenko plots was noted.[13c,d] This apparent increase beyond typical values of ≈3 m_e has not been satisfactorily explained. To do so is important because it implies that for a given carrier density, the Cu-containing materials have a larger *S*, potentially supporting improved *PF*. The m^*_{DOS} increase could be consistent with the emergence of a second band, doubling the orbital and valley degeneracy to $N_v = 6$, which using $m^*_{DOS} = N_v^{2/3} m^*_b$,[15] predicts a similar increase to that observed. Here, m^*_b is the band mass of the parabolic band. However, the emergence of such a second band is not realistic given the low concentration of Cu in the material ($y \leq 0.1$). The results of Density Functional Theory supercell calculations for $TiNiCu_ySn$ ($y = 0.05$ and 0.125) are shown in Figure 1f,g and show the emergence of a "fractured" conduction band with split bands at the X-point in the Brillouin zone, with a much stronger impact for the calculation with the larger concentration of the Cu interstitials. This modification of the electronic structure can be expected to impact the electronic transport compared to the ideal TiNiSn parent material. The equivalent calculation for X = Zr and Hf ($y = 0.125$) is shown in Figure S1 (Supporting Information) and shows that a very similar band fracturing occurs. The fracturing is therefore caused by the presence of the Cu interstitials and occurs for all X metals, with only minor differences between X metals.

In this work, we elucidate the origin of the enhanced *S* in the $XNiCu_ySn$ system and show that this effect can be controlled by adjusting the X-content. In addition, we show that compared to calculations based on pristine XNiSn materials, an *S* enhancement is always present, for any X-site composition.

2.2. Materials Synthesis and Characterization

To explore the evolution of the enhanced *S* and its link to composition, a total of 12 $XNiCu_ySn$ samples, including the X = Ti, Zr, and Hf endmembers, and several alloyed compositions were prepared using the route of arc melting, annealing, hot pressing, and annealing, using a temperature of 900 °C and slow cooling of the final hot-pressed disks. The Cu content ($0.0175 \leq y \leq 0.04$) was chosen in the expected region of optimal *PF*.

Full details of the synthetic procedure and sample characterization are given in the Supporting Information (SI). All samples have good purity with Rietveld analysis of X-ray diffraction data confirming the inclusion of most of the Cu as interstitials (Figures S2 and S3, Supporting Information). Crystallographic data are summarized in Tables S1 and S2 (Supporting Information). The Hall carrier concentrations confirm the highly doped

K. Domosud, K. Refson
Department of Physics
Royal Holloway University London
Egham TW20 0EX, UK

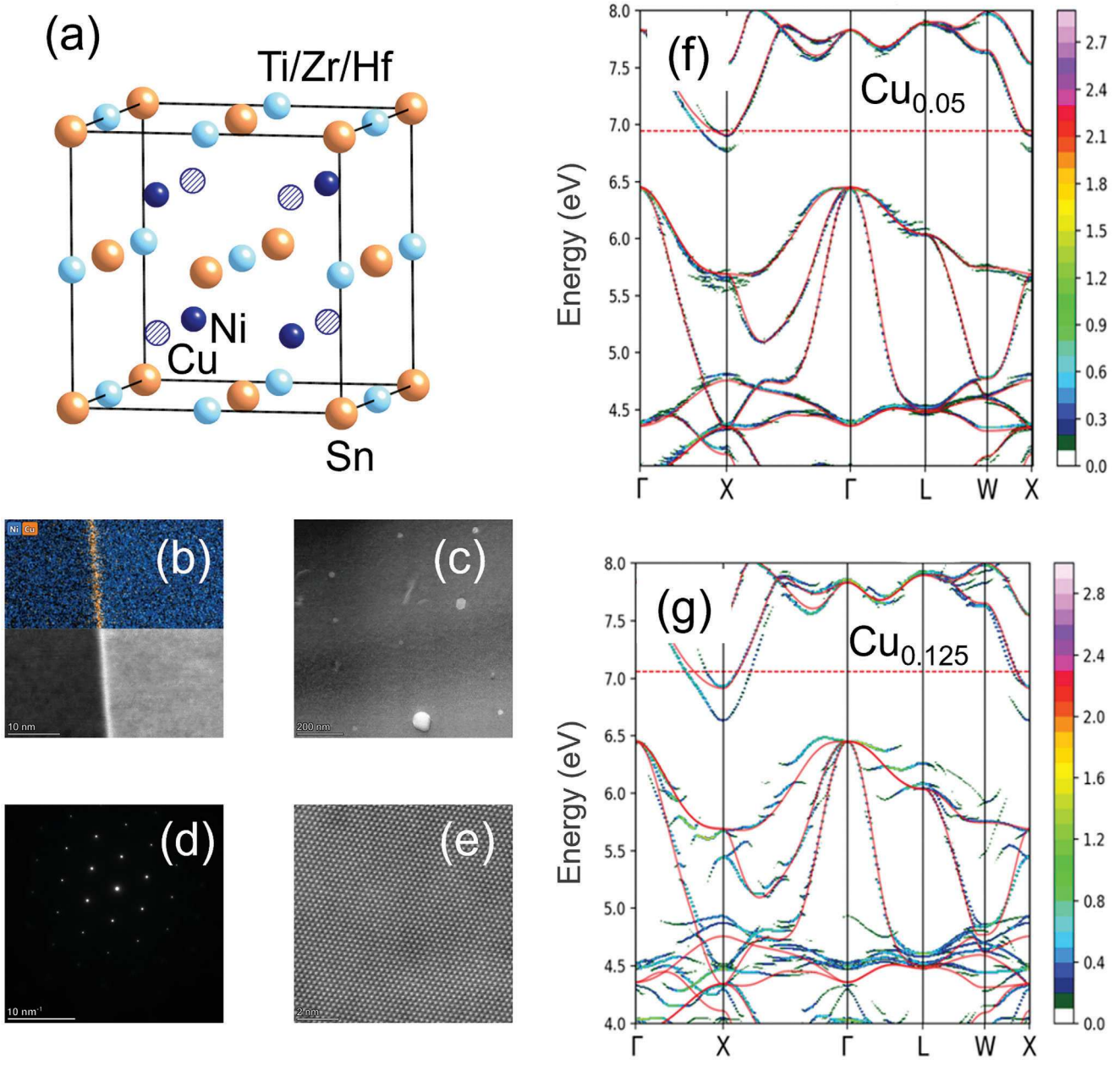

Figure 1. Structure and electronic bandstructure of the $XNiCu_ySn$ materials. a) HH unit cell highlighting the location of the X-site alloying elements (Ti, Zr, Hf) and interstitial Cu atoms. (b–e) TEM characterization of $TiNiCu_{0.03}Sn$: b) EDX (top) and corresponding HAADF (bottom) images across a grain boundary, showing Cu segregation forming a layer ≈1.6 nm thick. c) HAADF image showing several Cu inclusions distributed throughout a grain. Assuming a homogeneous distribution, a number density of ≈17–18 μm^{-2} is estimated. Their radii vary in the range of ≈20–70 nm. d) SAD and (e) atomic resolution HAADF from a region free of inclusions and oriented on the <111> zone axis, revealing a highly ordered structure without extended defects. f,g) Unfolded electronic band structure illustrating the emergence of a "fractured" conduction band at the X-point for 5% ($y = 0.05$) and 12.5% ($y = 0.125$) Cu interstitials. The value of 1 on the color bar corresponds to a single nondegenerate band per energy interval. The continuous red line is the band structure for pristine TiNiSn. The bandstructure of $y = 0.125$ is reproduced under terms of the CC-BY license.[13c] 2019, S.A. Barczak et al, published by the Royal Society of Chemistry.

nature of the samples, consistent with most Cu being present as interstitials and occupying the 4d site (Table S3, Supporting Information).

The results of regular SPB analysis are summarized in **Figure 2**. The Pisarenko plot in Figure 2a reveals that the $XNiCu_ySn$ samples have m^*_{DOS} values between 3–4 m_e. Compositions close to $TiNiCu_ySn$, including samples with ≲30% Zr or Hf alloying, have m^*_{DOS} ≈4 m_e, all toward the upper limit of observed values. By contrast, the other endmember compositions, $ZrNiCu_ySn$ and $HfNiCu_ySn$, are found to have regular m^*_{DOS} ≈3 m_e. Alloyed compositions based on these endmembers ($Zr/HfNiCu_ySn$ with <50% Ti) show only moderately increased m^*_{DOS} < 3.3 m_e.

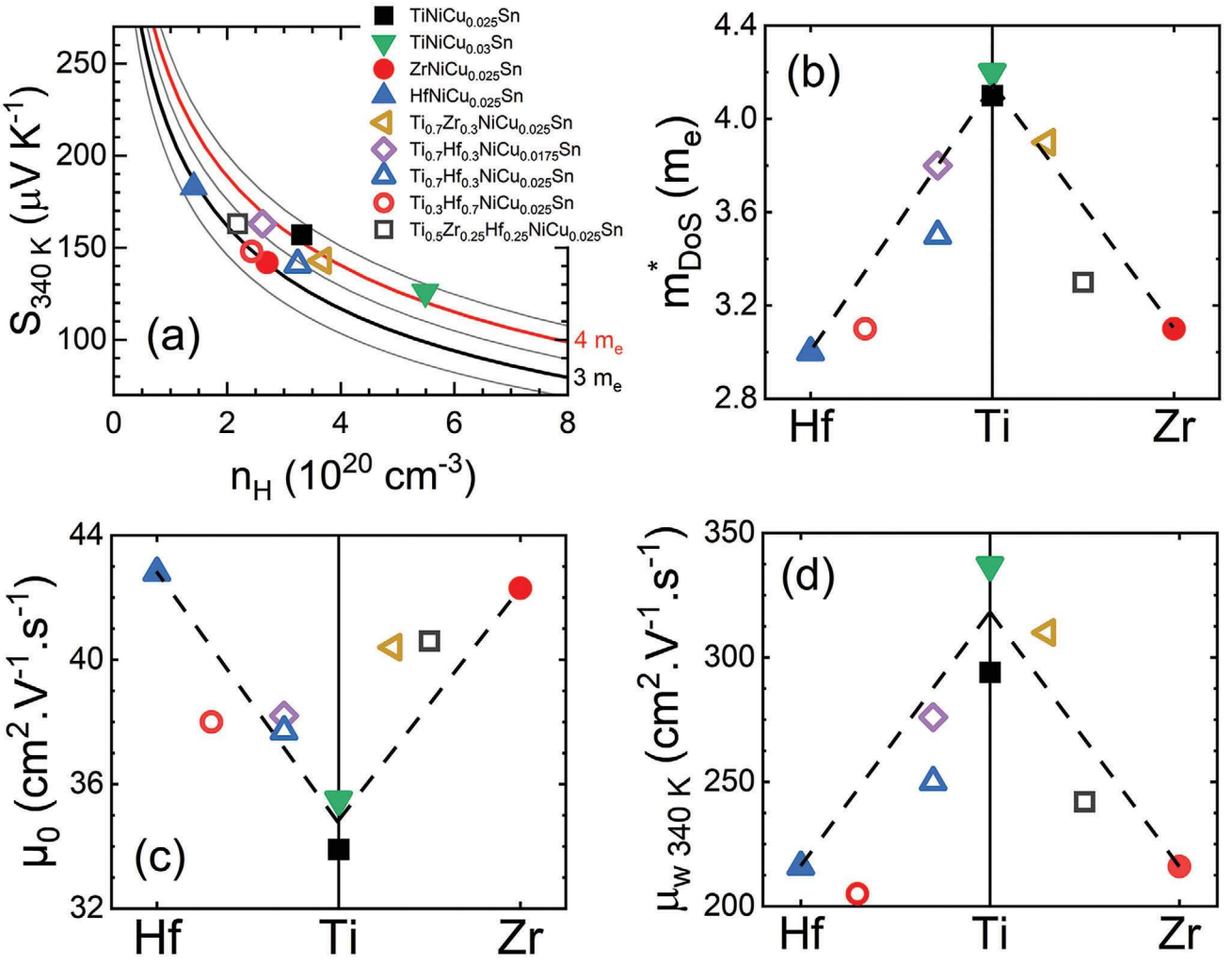

Figure 2. Conventional single parabolic band analysis for the $XNiCu_ySn$ materials. a) shows the Pisarenko plot of Seebeck coefficient *(S)* against carrier density (n_H) (b) shows the density of state effective mass (m^*_{DOS}), c) shows the mobility in the intrinsic limit (μ_0) and (d) shows the weighted mobility [$\mu_w = \mu_0.(m^*_{DOS}/m_e)^{3/2}$], which measures the overall electronic quality of the material and is a measure of the achievable *PF*. Ti-rich $XNiCu_ySn$ samples have the best electronic properties, caused by their large m^*_{DOS} with only moderately reduced μ_0.

Figure 2b shows the change in m^*_{DOS} plotted against X-site composition, revealing a clear maximum for $TiNiCu_ySn$ and ≤30% Zr or Hf alloyed samples. Hence, these samples have a larger *S* at a given carrier density. The impact of the X-site composition on mobility can be assessed using the intrinsic SPB mobility in the zero-carrier density limit (μ_0). This is obtained from the measured Hall mobility (μ_H) by assuming acoustic phonon scattering and allows the mobilities of samples with different carrier densities to be compared. The calculated μ_0 is plotted in Figure 2c and reveals that the samples with the enhanced *S* ($TiNiCu_ySn$, and ≤30% Zr/Hf alloyed), only have a 10–20% reduction in mobility, compared to samples with regular *S*. Overall, this favorable scenario leads to improved weighted mobilities, $\mu_w = \mu_0(m^*_{DOS}/m_e)^{3/2}$, shown in Figure 2d. The μ_w is a measure of the electronic quality of the material and a predictor of the maximum achievable *PF*. Hence, the SPB analysis shows that the favorable impact of the enhanced *S* is not offset by a strong reduction in carrier mobility and should be helpful in attaining improved *PF*.

The link between enhanced *S*, σ and its impact on *PF* is further analyzed in **Figure 3**, which shows log(*S*)-log(σ) and *PF*-σ plots at 340 K and 793 K. For degenerate samples, such as the $XNiCu_ySn$ materials reported here, $S \propto \sigma^{-1/s}$, where *s* gives information about the dominant scattering mechanism.[16] At 340 K (Figure 3a), the data fall between two parallel trendlines, the highest of which is fixed by samples with enhanced *S*, and the lower by samples with regular *S*. In terms of *S*, $TiNiCu_ySn$ and the ≤30% Zr or Hf alloyed samples show similar enhancements. However, a discrepancy occurs because the Hf alloyed samples have somewhat lower mobilities (Figure 2c). Hence, the $Ti_{0.7}Hf_{0.3}NiCu_ySn$ samples have lower σ and move away from the ideal *S*-σ trendline but remain superior to the $Zr/HfNiCu_{0.025}Sn$ samples with regular *S*. Figure 3b confirms that the *PF* for samples with enhanced *S* is much larger than the values found for samples with regular *S*. The *PF* increases from lowest values ≈2.2 mW m^{-1} K^{-2} ($Zr/HfNiCu_{0.025}Sn$ and $Ti_{0.3}Hf_{0.7}NiCu_{0.025}Sn$) to highest values of ≈3.5 mWm^{-1} K^{-2}

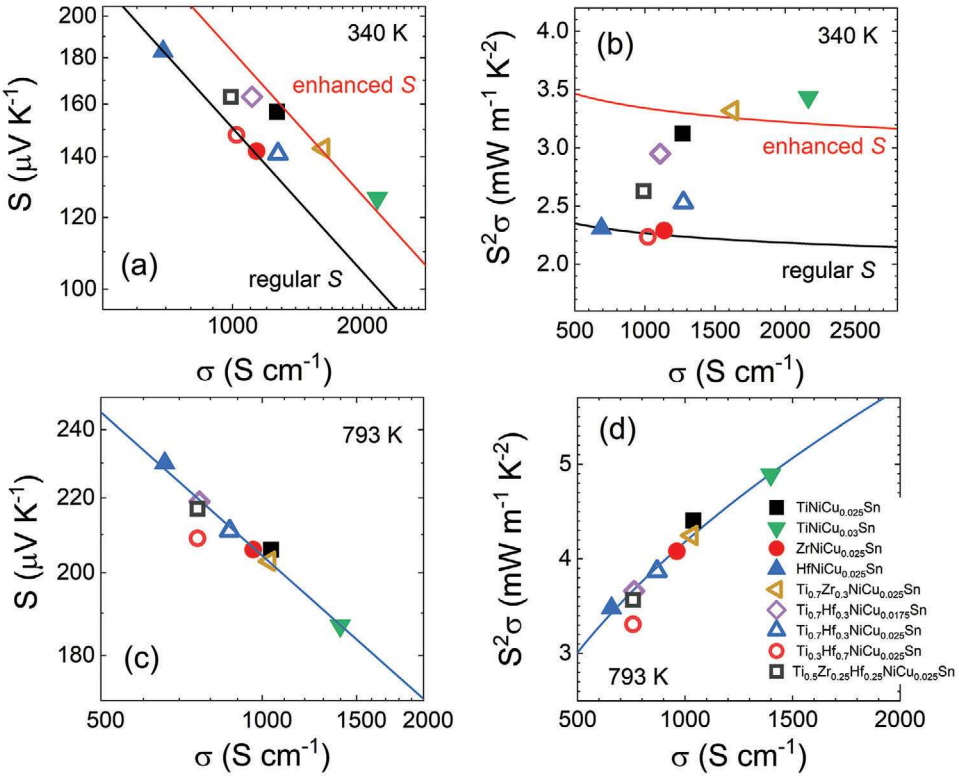

Figure 3. Seebeck (S) versus electrical conductivity (σ) analysis for the $XNiCu_ySn$ materials. Panels (a-b) show log-log plots of S-σ and linear plots of power factor, $PF = S^2\sigma$-σ at 340 K. Panels (c-d) show the equivalent plots at 793 K. At 340 K, the data falls between two parallel $S \propto \sigma^{(-1/s)}$ trendlines, corresponding to samples with the enhanced and regular S (m^*_{DOS}) from the Pisarenko analysis. The enhanced S leads to strongly improved PF, increasing by 40–50% for samples that fall on the regular S and enhanced S trendlines. At 793 K, all samples fall on single $S \propto \sigma^{(-1/s)}$ and PF-σ trendlines, indicating a more similar response between samples. Nevertheless, the $TiNiCu_ySn$ and $Ti_{0.7}Zr_{0.3}NiCu_{0.025}Sn$ samples maintain the highest PF, with $ZrNiCu_{0.025}Sn$ becoming more competitive.

($TiNiCu_ySn$ and $Ti_{0.7}Zr_{0.3}NiCu_{0.25}Sn$), an improvement of ≈50% (Figure 3b). The $Ti_{0.7}Hf_{0.3}NiCu_ySn$ samples have $PF = 2.5$–3 mW m^{-1} K^{-2}. The PF of $Ti_{0.5}Zr_{0.25}Hf_{0.25}NiCu_{0.025}Sn$ also falls in this range, despite only having a small enhancement of S (Figure 2a), but this sample benefits from a higher mobility (Figure 2c). At 793 K (Figure 3c), all samples fall on a single $S \propto \sigma^{-1/s}$ trendline and the clear distinction between compositions with enhanced and regular S disappears. In terms of PF, $TiNiCu_ySn$ and $Ti_{0.7}Zr_{0.3}NiCu_{0.25}Sn$ have the largest values (Figure 3d), but $ZrNiCu_ySn$ now approaches within 20–25%, with values near 5 and 4 mW m^{-1} K^{-2} respectively. The converging trend in electronic properties is also evident from the temperature dependence of μ_w shown in Figure S4 (Supporting Information), where the difference between samples is much smaller at high temperatures.

To summarize: a significant enhancement of S is found for $TiNiCu_ySn$ and ≤30% Zr or Hf alloyed samples (m^*_{DOS} ≈4 m_e), whereas Zr/$HfNiCu_ySn$ samples have S values in line with typical literature values (m^*_{DOS} ≈3m_e). Alloyed compositions close to Zr/$HfNiCu_ySn$ (<50% Ti) only show modest improvements in S (m^*_{DOS} <3.3 m_e). These S enhancements translate to PF improvements as the carrier mobilities are only slightly reduced. In prior works, improvements in S have been linked to band convergence, resonant states, and carrier filtering effects in composite samples.[3b] However, the main feature in our band-structure calculations is the fracturing of the conduction band. There is no evidence for band convergence and or the emergence of resonant states. Despite the presence of segregated Cu, in the form of metallic inclusions and Cu-enriched grain boundaries, these are at low number densities, making it unlikely that they influence the electronic structure substantially. Instead, we propose that the fracturing of the conduction band and the introduction of split impurity bands drive the S enhancement. This mechanism acts throughout the material as it is linked to the unit cell composition and can explain the observed experimental trends.

2.3. Modeling of Dopant Bands

To model the fractured bandstructure of the $XNiCu_ySn$ materials we include a "dopant band" of finite extent and perform energy dependent transport simulations utilizing the Boltzmann Transport Equation (BTE). This band has a variable extent, dispersion, and offset with respect to the conduction band of the pristine XNiSn parent materials. This arrangement is schematically illustrated in **Figure** 4a,b for the bands and DOS, respectively. We label this second band an impurity (or dopant) band as it is linked to the introduction of interstitial Cu dopants that are introduced in low concentrations.

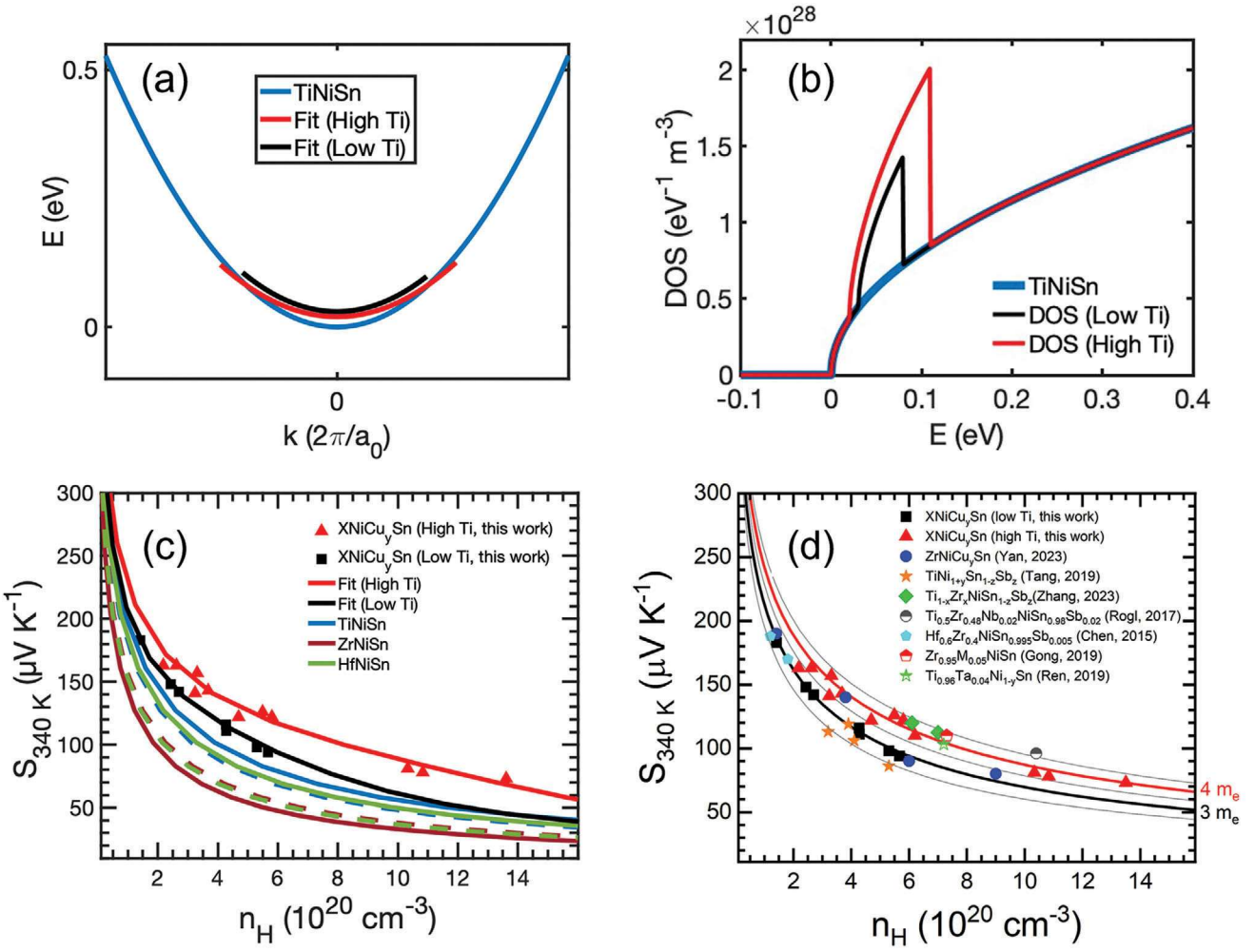

Figure 4. Energy-dependent band analysis – enhancement of the Seebeck coefficient (*S*) via dopant-derived impurity bands. a) The band diagram of the basis material (TiNiSn) with added dopant states. b) The change in total DOS is due to the dopant states. c) The enhancement in *S* of measured data with respect to the pristine material simulations. Blue, brown, and green lines are Pisarenko plots simulated for pristine HHs for two different mass values.[17] Fits were made for $XNiCu_ySn$ samples with ≥50% Ti (red triangles) and <50% Ti on the X site (black squares) cases. The increase in *S* in the Pisarenko plot (c), due to impurity states, has a similar effect as an increase in the m^*_{DOS} would have. d) Pisarenko plot comparing a range of XNiSn materials from the literature, which exhibits both regular and enhanced *S*. Data taken from Refs.[7b,e,g,i,13c,d,18]

To start, the experimental Pisarenko (S-n_H) data was compared to pristine TiNiSn, ZrNiSn, and HfNiSn, using two sources of m^*_{DOS} from the literature,[17] to accommodate for uncertainties (Table S4, Supporting Information). The detailed procedure is outlined in the SI and the different *S* are plotted in Figure 4c for the three materials (different colored lines) and the two different m^*_{DOS} sources (solid versus dashed lines). The experimental data used for fitting includes the $XNiCu_ySn$ samples prepared in this study and a set of earlier samples with properties summarized in Table S5 (Supporting Information). These were divided up into $XNiCu_ySn$ samples with ≥50% Ti (significant *S* enhancements observed) and <50% Ti (no or small *S* enhancement) on the X site. In all cases, including for the <50% Ti samples where no *S* enhancement is found, the Pisarenko lines are below the experimental data, confirming that an enhancement is needed to match the measured data. As can be seen in Figure 4c, the effect is significant with 20–50% higher *S* values, even when comparing to the nearest Pisarenko line. This implies that compared to pristine XNiSn all experimental samples, including $Zr/HfNiCu_ySn$, have enhanced *S* values. We propose that even for materials with low m^*_{DOS} ≈3m_e from SPB analysis, impurity bands are already making a significant contribution. Next, a dopant band was introduced using TiNiSn as the basis, forming the two-band system shown in Figure 4a. The extent of the dopant band, its effective mass, and placement in energy, translates to additional states of a certain height, broadening, and energy positioning in the DOS of the material as shown in Figure 4b. This modified electronic structure was used within the BTE model, accounting for inter-band scattering, and *S* was extracted. By adjusting the height, width, and energy of these bands, the experimental data for both the ≥50% Ti (red lines in Figure 4c) and <50% Ti on the X site cases (black lines) can be matched with relatively minor changes to the dopant band (fit parameters are summarized in Table S6, Supporting Information).

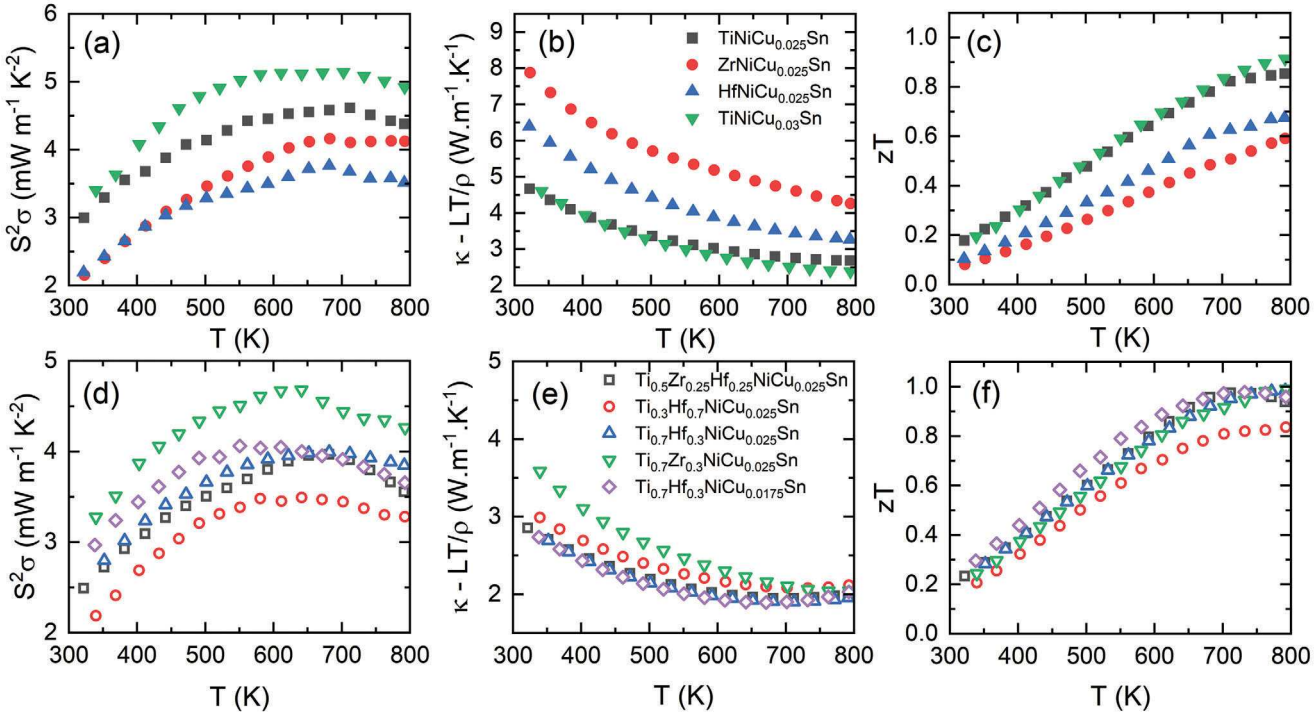

Figure 5. Overview of key thermoelectric properties of the XNiCu$_y$Sn materials. Panels give the TE power factor ($PF = S^2\sigma$), lattice thermal conductivity (κ-LT/ρ), and figure of merit (zT) for the end members (a–c) and alloyed (d–f) compositions. The full TE properties are given in the supporting information.

In effect, the dopant band has the same influence on the Pisarenko lines as an increase in the m^*_{DOS} of the material. However, rather than being caused by increased degeneracy (N_v) or band mass (m^*_b), it can be quantitively attributed to the presence of a dopant-derived band of finite extent. These dopant bands are present in all XNiCu$_y$Sn samples, but alignment is most favorable in case of TiNiSn and hence the largest S enhancements are observed. A key feature is that the impurity bands retain dispersion, that is, the carriers do not become localized, which is consistent with the largely conserved mobility that is observed experimentally. This behavior contrasts with interstitial Ni, which leads to flat bands in the bandgap, causing Fermi level pinning and reduced mobilities.[18,19] As already mentioned, an important aspect of the model is that small changes in energy offset, dispersion, and extent of the dopant band are sufficient to explain measured variations in S for all our XNiCu$_y$Sn compositions. Indeed, beyond the samples presented in this manuscript, the literature shows evidence for S enhancement, as illustrated by the Pisarenko plot in Figure 4d. This shows experimental S-n_H data for a wide range of XNiSn samples, with various dopants and alloying elements, which are found to have SPB m^*_{DOS} values between 3–4.5 m$_e$. This suggests that dopant-derived impurity bands are widely present and influence TE transport.

2.4. Thermoelectric Performance of the XNiCu$_y$Sn Materials

The temperature dependence of the PF, κ_L, and zT for the XNiCu$_y$Sn samples are shown in **Figure 5**, with the complete set of TE data given in Figures S5 and S6 (Supporting Information).

TiNiCu$_{0.03}$Sn has the best overall PF, achieving the highest value of 5.2 mW m^{-1} K^{-2} with values close to this over a broad range of 500–793 K. Out of the end-member compositions, it also has the lowest $\kappa_L \approx 5$ W m^{-1} K^{-1} near room temperature. This enables a promising $zT = 0.9$ at 793 K, in a composition that has no alloying, with the low κ_L due to the Cu interstitial dopants.[13b] The lower doped TiNiCu$_{0.025}$Sn composition has a broad PF plateau near 4.5 mW m^{-1} K^{-2} and achieves a similar $zT = 0.85$ at 793 K. As discussed, the lack of S enhancement means that ZrNiCu$_{0.025}$Sn and HfNiCu$_{0.025}$Sn have the lowest $S^2\sigma$ near room temperature. Upon heating, ZrNiCu$_{0.025}$Sn achieves a plateau of ≈4 mW m^{-1} K^{-2} with HfNiCu$_{0.025}$Sn reaching ≈3.5 mW m^{-1} K^{-2}. ZrNiCu$_{0.025}$Sn has the largest κ_L of the endmembers, followed by HfNiCu$_{0.025}$Sn, which follows the expected trend based on Cu dopant solubility limit and average atomic mass.[17b] Peak zT = 0.6 (Hf) and $zT = 0.5$ (Zr) are reached at 793 K, which is substantially lower than found for the TiNiCu$_y$Sn compositions, but in line with results on Sb doped samples.

The Ti$_{0.7}$Zr$_{0.3}$NiCu$_{0.025}$Sn sample has the highest PF of the alloyed composition, with a plateau of ≈4.5 mW.m^{-1}.K^{-2}, which is comparable to the TiNiCu$_{0.025}$Sn sample. Its PF near room temperature is also very high (>3 mW.m^{-1}.K^{-2}) and comparable to the TiNiCu$_{0.03}$Sn sample. The 30% Hf alloyed samples have lower peak PF, with both Ti$_{0.7}$Hf$_{0.3}$NiCu$_y$Sn samples reaching plateaus of ≈4 mW m^{-1} K^{-2} (with the PF peaking at lower temperature for the lower doped $y = 0.0175$ sample). The 70% Hf alloyed Ti$_{0.3}$Hf$_{0.7}$NiCu$_{0.025}$Sn sample only reaches ≈3.3 mW m^{-1} K^{-2} at high temperature, linked to the lack of S enhancement and strong bipolar transport. In terms of alloying efficiency, heavy Hf leads to large reductions in κ_L. The regular alloying

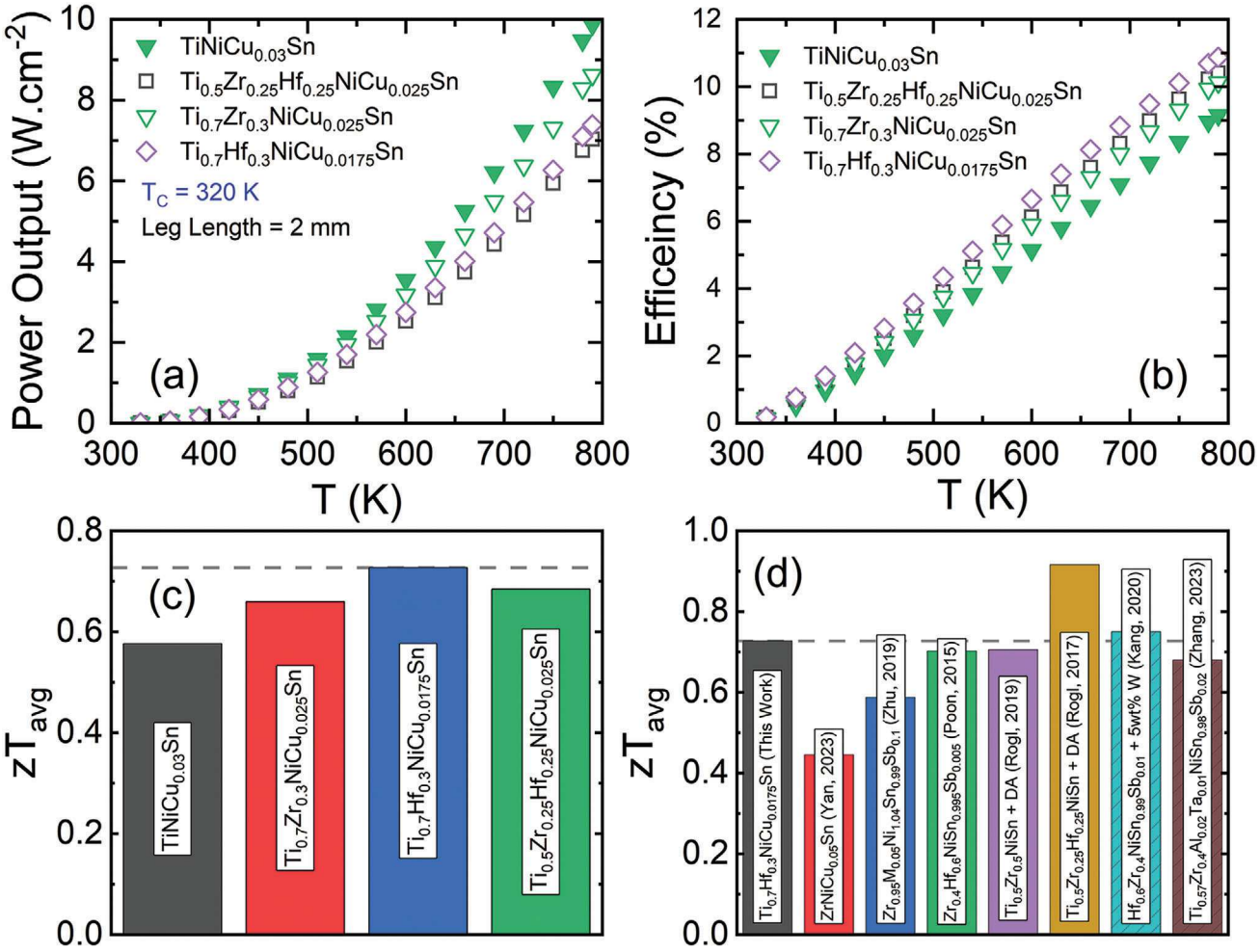

Figure 6. Single-leg device performance for selected $XNiCu_ySn$ materials and comparison to the state-of-the-art. Panel (a) shows the power output and (b) shows the efficiency for a 2 mm single leg device with a cold side of 320 K. (c, d) best temperature averaged figures of merit (zT_{avg}) achieved in our work (320–793 K), compared to some of the best literature values for other n-type XNiSn systems.[7b,d,g–i,13d] The $XNiCu_ySn$ samples reach state-of-the art zT_{avg} values, despite the lack of intense processing, and are only clearly exceeded by studies where a densification agent (DA) was used.

dependence of mixing Ti-Hf is confirmed in Figure S7 (Supporting Information), whilst higher Cu doping levels reduce bipolar transport (Figure S8, Supporting Information). All 30% alloyed samples ($Ti_{0.7}Zr_{0.3}NiCu_{0.025}Sn$, $Ti_{0.7}Hf_{0.3}NiCu_{0.0175}Sn$, and $Ti_{0.7}Hf_{0.3}NiCu_{0.025}Sn$) reach the critical benchmark of zT = 1 above 700 K (Figure 5f). The $Ti_{0.5}Zr_{0.25}Hf_{0.25}NiCu_{0.025}Sn$ sample with mixed Ti/Zr/Hf alloying achieves a similar low κ_L to the Ti-Hf alloyed samples. At low temperatures, a moderate $S^2\sigma$ ≈2.6 mW m^{-1} K^{-2} is found (in keeping with the only slightly enhanced S), improving to a plateau ≈4 mW m^{-1} K^{-2} at high temperature, that is, comparable to $ZrNiCu_{0.025}Sn$ and the $Ti_{0.7}Hf_{0.3}NiCu_ySn$ samples. This sample also achieves zT = 1 above 700 K, due to its low κ_L and moderate PF (Figure 5f).

Resonant ultrasound spectroscopy measurements reveal that alloying and interstitial Cu dopants have negligible impact on the elastic moduli (Table S7, Supporting Information). The observed low κ_L is therefore due to structural disorder caused by the dopants and alloying and not by large changes in chemical bonding.

Finally, we present a comparison of the Cu containing materials to literature data on XNiSn samples. In **Figure 6**a,b, the temperature-averaged PF and zT are used to calculate theoretical device power outputs and efficiencies for our materials.[5] Improved near ambient performance substantially improves the temperature-averaged properties that are important for device applications. For example, the large PF achieved in $TiNiCu_{0.03}Sn$ translates directly to the largest potential power output of ≈10 W.cm^{-2} between 320–790 K. The large zT_{avg} value aided by maximization of zT close to room temperature allows $Ti_{0.7}Hf_{0.3}NiCu_{0.0175}Sn$ to have the largest theoretical efficiency of ≈11% between 320–790 K, despite having a 50% lower power generation potential compared to $TiNiCu_{0.03}Sn$. It is worth noting that these calculations present an upper limit as parasitic contact resistances and warming up of the cold side are not considered. Figure 6c,d shows the zT_{avg} values for the samples of this manuscript and a comparison to literature samples. This reveals highly promising zT_{avg} = 0.58 for $TiNiCu_{0.03}Sn$, zT_{avg} = 0.67 for $Ti_{0.7}Zr_{0.3}NiCu_{0.025}Sn$, and zT_{avg} = 0.72 for $Ti_{0.7}Hf_{0.3}NiCu_{0.0175}Sn$.

These values are competitive with the best reported n-type XNiSn materials, which in most cases have benefitted from many optimization studies and extensive processing.

3. Conclusion

We demonstrate the presence of a new mechanism for *S* and *PF* enhancement of TE materials, different from band convergence. We attribute this effect to the dopant-induced fracturing of the conduction band, leading to impurity bands of finite extent. These bands, with the correct energy offset, dispersion, and extent with respect to the parent material, lead to enhanced *S*, independent of the carrier density. The dispersive character of the dopant-bands allows for retaining mobility, enabling *PF* improvements of the order of 50%, which is very comparable with other methods such as band convergence. Importantly, dopant bands and their positive impact on the *PF* can appear in single pocket materials, where band convergence is not possible. Further understanding and controlling the synergistic interaction between host-and dopant-bands provides a new development direction for improving the *PF* of TE materials.

Experimental Section

The experimental procedures are described in the supporting information.

Supporting Information

Supporting Information is available from the Wiley Online Library or from the author.

Acknowledgements

The EPSRC is acknowledged for support under award EP/N01717X/1, EP/N01703X/1, EP/X02346X/1, EP/L017008/1, EP/R023751/1 and EP/T019298/1 and for a PhD studentship for S.A.B.

Conflict of Interest

The authors declare no conflict of interest.

Data Availability Statement

The research data supporting this publication can be accessed at https://doi.org/10.17630/7e1f8a90-1785-4d8b--a2e2-32c7c503b820.

Keywords

band engineering, half-heusler thermoelectrics, impurity bands, Seebeck effect, TiNiSn

Received: November 8, 2024
Revised: December 18, 2024
Published online:

[1] a) Q. Y. Yan, M. G. Kanatzidis, *Nat. Mater.* **2022**, *21*, 503; b) J. He, T. M. Tritt, *Science.* **2017**, *357*, eaak9997; c) D. M. Rowe, *Materials, Preparation, and Characterization in Thermoelectrics*, CRC Press, Boca Raton, **2012**. d) G. J. Snyder, E. S. Toberer, *Nat. Mater.* **2008**, *7*, 105.
[2] J. Mao, G. Chen, Z. F. Ren, *Nat. Mater.* **2021**, *20*, 454.
[3] a) X.-L. Shi, J. Zou, Z.-G. Chen, *Chem. Rev.* **2020**, *120*, 7399; b) T. J. Zhu, Y. T. Liu, C. G. Fu, J. P. Heremans, J. G. Snyder, X. B. Zhao, *Adv. Mater.* **2017**, *29*, 1605884; c) S. K. Yee, S. LeBlanc, K. E. Goodson, C. Dames, *Energy Environ. Sci.* **2013**, *6*, 2561.
[4] a) B. B. Jiang, W. Wang, S. X. Liu, Y. Wang, C. F. Wang, Y. N. Chen, L. Xie, M. Y. Huang, J. Q. He, *Science.* **2022**, *377*, 208; b) L. Z. Su, D. Y. Wang, S. N. Wang, B. C. Qin, Y. P. Wang, Y. X. Qin, Y. Jin, C. Chang, L. D. Zhao, *Science.* **2022**, *375*, 1385; c) S. Roychowdhury, T. Ghosh, R. Arora, M. Samanta, L. Xie, N. K. Singh, A. Soni, J. Q. He, U. V. Waghmare, K. Biswas, *Science.* **2021**, *371*, 722; d) B. B. Jiang, Y. Yu, J. Cui, X. X. Liu, L. Xie, J. C. Liao, Q. H. Zhang, Y. Huang, S. C. Ning, B. H. Jia, B. Zhu, S. Q. Bai, L. D. Chen, S. J. Pennycook, J. Q. He, *Science.* **2021**, *371*, 830; e) C. J. Zhou, Y. K. Lee, Y. Yu, S. Byun, Z. Z. Luo, H. Lee, B. Z. Ge, Y. L. Lee, X. Q. Chen, J. Y. Lee, O. Cojocaru-Miredin, H. Chang, J. Im, S. P. Cho, M. Wuttig, V. P. Dravid, M. G. Kanatzidis, I. Chung, *Nat. Mater.* **2021**, *20*, 1378; f) C. Chang, M. H. Wu, D. S. He, Y. L. Pei, C. F. Wu, X. F. Wu, H. L. Yu, F. Y. Zhu, K. D. Wang, Y. Chen, L. Huang, J. F. Li, J. Q. He, L. D. Zhao, *Science.* **2018**, *360*, 778; g) L. D. Zhao, G. J. Tan, S. Q. Hao, J. Q. He, Y. L. Pei, H. Chi, H. Wang, S. K. Gong, H. B. Xu, V. P. Dravid, C. Uher, G. J. Snyder, C. Wolverton, M. G. Kanatzidis, *Science.* **2016**, *351*, 141; h) S. I. Kim, K. H. Lee, H. A. Mun, H. S. Kim, S. W. Hwang, J. W. Roh, D. J. Yang, W. H. Shin, X. S. Li, Y. H. Lee, G. J. Snyder, S. W. Kim, *Science.* **2015**, *348*, 109.
[5] a) H. S. Kim, W. Liu, Z. Ren, *Energy Environ. Sci.* **2017**, *10*, 69; b) G. J. Snyder, A. H. Snyder, *Energy Environ. Sci.* **2017**, *10*, 2280.
[6] a) R. J. Quinn, J.-W. G. Bos, *Mater. Adv.* **2021**, *2*, 6246; b) T. Zhu, C. Fu, H. Xie, Y. Liu, X. Zhao, *Adv. Energy Mater.* **2015**, *5*, 1500588.
[7] a) Q. H. Lou, Z. H. Gao, S. Han, F. Liu, C. G. Fu, T. J. Zhu, *Adv. Energy Mater.* **2024**, *14*, 2402399; b) X. Zhang, M. Huang, H. Li, J. Chen, P. Xu, B. Xu, Y. Wang, G. Tang, S. Yang, *J. Mater. Chem. A.* **2023**, *11*, 8150; c) J. J. Yu, Y. F. Xing, C. L. Hu, Z. J. Huang, Q. Y. Qiu, C. Wang, K. Y. Xia, Z. Y. Wang, S. Q. Bai, X. B. Zhao, L. D. Chen, T. J. Zhu, *Adv. Energy Mater.* **2020**, *10*, 2000888; d) H. B. Kang, B. Poudel, W. Li, H. Lee, U. Saparamadu, A. Nozariasbmarz, M. G. Kang, A. Gupta, J. J. Heremans, S. Priya, *Mater. Today.* **2020**, *36*, 63; e) B. Gong, Y. Li, F. Liu, J. Zhu, X. Wang, W. Ao, C. Zhang, J. Li, H. Xie, T. Zhu, *ACS Appl. Mater. Interfaces.* **2019**, *11*, 13397; f) Y. Liu, C. Fu, K. Xia, J. Yu, X. Zhao, H. Pan, C. Felser, T. Zhu, *Adv. Mater.* **2018**, *30*, 1800881; g) G. Rogl, P. Sauerschnig, Z. Rykavets, V. V. Romaka, P. Heinrich, B. Hinterleitner, A. Grytsiv, E. Bauer, P. Rogl, *Acta Mater.* **2017**, *131*, 336; h) M. Gürth, G. Rogl, V. V. Romaka, A. Grytsiv, E. Bauer, P. Rogl, *Acta Mater.* **2016**, *104*, 210; i) L. Chen, S. Gao, X. Zeng, A. Mehdizadeh Dehkordi, T. M. Tritt, S. J. Poon, *Appl. Phys. Lett.* **2015**, *107*, 041902.
[8] a) Z. H. Gao, K. Y. Xia, P. F. Nan, L. Yin, C. L. Hu, A. R. Li, S. Han, M. Zhang, M. Z. Chen, B. H. Ge, Q. Zhang, C. G. Fu, T. J. Zhu, *Small.* **2023**, *19*, 2302457; b) K. Y. Xia, Y. T. Liu, S. Anand, G. J. Snyder, J. Z. Xin, J. J. Yu, X. B. Zhao, T. J. Zhu, *Adv. Funct. Mater.* **2018**, *28*, 1705845.
[9] a) M. Mitra, A. Benton, M. S. Akhanda, J. Qi, M. Zebarjadi, D. J. Singh, S. J. Poon, *Mater. Today Phys.* **2022**, *28*, 100900; b) C. Hu, K. Xia, X. Chen, X. Zhao, T. Zhu, *Mater. Today Phys.* **2018**, *7*, 69.
[10] a) R. B. Villoro, D. Zavanelli, C. W. Jung, D. A. Mattlat, R. H. Naderloo, N. Pérez, K. Nielsch, G. J. Snyder, C. Scheu, R. He, S. Y. Zhang, *Adv. Energy Mater.* **2023**, *13*, 2204321; b) W. J. Li, B. Poudel, R. A. Kishore, A. Nozariasbmarz, N. Liu, Y. Zhang, S. Priya, *Adv. Mater.* **2023**, *35*, 2210407; c) H. Zhu, J. Mao, Y. Li, J. Sun, Y. Wang, Q. Zhu, G. Li, Q. Song, J. Zhou, Y. Fu, R. He, T. Tong, Z. Liu, W. Ren, L. You, Z. Wang, J.

Luo, A. Sotnikov, J. Bao, K. Nielsch, G. Chen, D. J. Singh, Z. Ren, *Nat. Commun.* **2019**, *10*, 270; d) J. Yu, C. Fu, Y. Liu, K. Xia, U. Aydemir, T. C. Chasapis, G. J. Snyder, X. Zhao, T. Zhu, *Adv. Energy Mater.* **2018**, *8*, 1701313; e) W. Y. Ren, H. T. Zhu, Q. Zhu, U. Saparamadu, R. He, Z. H. Liu, J. Mao, C. Wang, K. Nielsch, Z. M. Wang, Z. F. Ren, *Adv. Sci.* **2018**, *5*, 1800278; f) R. He, D. Kraemer, J. Mao, L. Zeng, Q. Jie, Y. C. Lan, C. H. Li, J. Shuai, H. S. Kim, Y. Liu, D. Broido, C. W. Chu, G. Chen, Z. Ren, *Proc. Natl. Acad. Sci. USA.* **2016**, *113*, 13576; g) C. G. Fu, H. J. Wu, Y. T. Liu, J. Q. He, X. B. Zhao, T. J. Zhu, *Adv. Sci.* **2016**, *3*, 1600035; h) C. G. Fu, S. Q. Bai, Y. T. Liu, Y. S. Tang, L. D. Chen, X. B. Zhao, T. J. Zhu, *Nat. Commun.* **2015**, *6*, 8144; i) C. Fu, T. Zhu, Y. Liu, H. Xie, X. Zhao, *Energy Environ. Sci.* **2015**, *8*, 216.

[11] a) X. Bao, K. J. Liu, W. H. Xue, H. H. Yao, X. J. Ma, X. F. Li, S. Ye, F. Cao, J. Mao, Q. Zhang, *Adv. Funct. Mater.* **2024**, *34*, 2404279; b) H. Zhu, R. He, J. Mao, Q. Zhu, C. Li, J. Sun, W. Ren, Y. Wang, Z. Liu, Z. Tang, A. Sotnikov, Z. Wang, D. Broido, D. J. Singh, G. Chen, K. Nielsch, Z. Ren, *Nat. Commun.* **2018**, *9*, 2497.

[12] S. Guo, S. Anand, M. K. Brod, Y. Zhang, G. J. Snyder, *J. Mater. Chem. A.* **2022**, *10*, 3051.

[13] a) R. A. Downie, R. I. Smith, D. A. MacLaren, J.-W. G. Bos, *Chem. Mater.* **2015**, *27*, 2449; b) S. A. Barczak, J. E. Halpin, J. Buckman, R. Decourt, M. Pollet, R. I. Smith, D. A. MacLaren, J.-W. G. Bos, *ACS Appl. Mater. Interfaces.* **2018**, *10*, 4786; c) S. A. Barczak, R. J. Quinn, J. E. Halpin, K. Domosud, R. I. Smith, A. R. Baker, E. Don, I. Forbes, K. Refson, D. A. MacLaren, J. W. G. Bos, *J. Mater. Chem. A.* **2019**, *7*, 27124; d) R. Yan, C. Shen, M. Widenmeyer, T. Luo, R. Winkler, E. Adabifiroozjaei, R. Xie, S. Yoon, E. Suard, L. Molina-Luna, H. Zhang, W. Xie, A. Weidenkaff, *Mater. Today Phys.* **2023**, *33*, 101049; e) Y. Lei, C. Yong, F. Gao, N. Wang, Y. Li, Z. Chen, D. Wang, *Mater. Today Commun.* **2024**, *40*, 109736.

[14] a) H. He, J. E. Halpin, S. R. Popuri, L. Daly, J.-W. G. Bos, M. P. Moody, D. A. MacLaren, P. A. Bagot, *Microsc. Microanal.* **2022**, *28*, 1340; b) J. E. Halpin, B. Jenkins, M. P. Moody, R. W. H. Webster, J.-W. G. Bos, P. A. J. Bagot, D. A. MacLaren, *ACS Appl. Electron. Mater.* **2022**, *4*, 4446.

[15] Y. Pei, H. Wang, G. J. Snyder, *Adv. Mater.* **2012**, *24*, 6125.

[16] S. D. Kang, G. J. Snyder, *Nat. Mater.* **2017**, *16*, 252.

[17] a) P. Graziosi, C. Kumarasinghe, N. Neophytou, *ACS Appl. Energy Mater.* **2020**, *3*, 5913; b) S. A. Barczak, *PhD Thesis*, Heriot-Watt University, Edinburgh, **2018**.

[18] a) Y. Tang, X. Li, L. H. J. Martin, E. Cuervo Reyes, T. Ivas, C. Leinenbach, S. Anand, M. Peters, G. J. Snyder, C. Battaglia, *Energy Environ. Sci.* **2018**, *11*, 311; b) W. Ren, H. Zhu, J. Mao, L. You, S. Song, T. Tong, J. Bao, J. Luo, Z. Wang, Z. Ren, *Adv. Electron. Mater.* **2019**, *5*, 1900166.

[19] Y. Sun, W. Qiu, L. Zhao, H. He, L. Yang, L. Chen, H. Deng, X. Shi, J. Tang, *Chem. Phys. Lett.* **2020**, *755*, 137770.